Hindawi
Advances in Materials Science and Engineering
Volume 2020, Article ID 4639382, 16 pages
https://doi.org/10.1155/2020/4639382

Research Article

A Modified Analytical Heat Source Model for Numerical Simulation of Temperature Field in Friction Stir Welding

Xiangqian Liu[1], **Yan Yu**[1], **Shengli Yang**[1] and **Huijie Liu**[2]

[1]*Luoyang Ship Material Research Institute, Luoyang 471023, China*
[2]*State Key Laboratory of Advanced Welding and Joining, Harbin Institute of Technology, Harbin 150001, China*

Correspondence should be addressed to Xiangqian Liu; liuxqhit@163.com

Received 18 August 2019; Revised 12 November 2019; Accepted 21 December 2019; Published 31 January 2020

Academic Editor: Stanislaw Dymek

In the conventional analytical model used for heat generation in friction stir welding (FSW), the heat generated at the pin/workpiece interface is assumed to distribute uniformly in the pin volume, and the heat flux is applied as volume heat. Besides, the tilt angle of the tool is assumed to be zero for simplicity. These assumptions bring about simulating deviation to some extent. To better understand the physical nature of heat generation, a modified analytical model, in which the nonuniform volumetric heat flux and the tilt angle of the tool were considered, was developed. Two analytical models are then implemented in the FEM software to analyze the temperature fields in the plunge and traverse stage during FSW of AA6005A-T6 aluminum hollow extrusions. The temperature distributions including the maximum temperature and heating rate between the two models are different. The thermal cycles in different zones further revealed that the peak temperature and temperature gradient are very different in the high-temperature region. Comparison shows that the modified analytical model is accurate enough for predicting the thermal cycles and peak temperatures, and the corresponding simulating precision is higher than that of the conventional analytical model.

1. Introduction

During friction stir welding (FSW), the heat derived from the friction and plastic deformation is the key factor that dictates the final weld quality [1–3]. It generally provides two primary functions [4, 5]: (i) making the metal material enough soft for the tool to stir to form the solid-state weld and (ii) resulting in the microstructural evolution to influence the joint properties. A precise heat measurement can give the specific peak temperature and thermal cycle to evaluate the weld quality, while large temperature gradient and intense plastic deformation in the stirred zone make it very difficult. Moreover, only limited temperature data can be obtained via experimental measurement [6]. As a contrast, the numerical models can be very efficient and convenient to give global and detailed thermal information [7].

Since the late 1990s, two main kinds of numerical models including computational fluid dynamic (CFD) model and computational solid mechanics (CSM) model have been developed. The CFD models can describe the thermomechanical interaction between the tool and workpiece, and the most important consideration in the frictional boundary condition is the determination of the contact state [8]. In many CFD models, the contact conditions at the tool/workpiece interface are considered as full sticking, which usually leads to an overestimation of peak temperature [8–10]. Atharifar et al. [11] assumed a sliding contact state during FSW, in which the velocity of material at the tool/workpiece interface was artificially defined as 60% of the tool velocity to investigate the loads carried by the tool. Chen et al. [12] presented a new frictional boundary condition based on an implementation of the Coulomb friction model, and the model yielded a nonuniform distribution of contact state over the interface. The sticking state was present over a large area at the tool-workpiece interface, while significant interfacial sliding occurs at the shoulder periphery, the lower part of

the pin side, and the periphery of the pin bottom. Moreover, the CFD models are based on the Eulerian method irrespective of time, and it is hard to simulate the temperature field and material flow varying with the time [8].

The CSM models can overcome the above-mentioned shortcomings, and the Lagrangian and the Arbitrary Lagrangian–Eulerian (ALE) formulations are mainly adopted. In most models using the ALE formulations, the grids are remeshed in the simulating process, and the tool/workpiece interaction including friction and plastic deformation can be defined to reflect the welding process to some extent. But excessive remeshing operations in the simulating process will employ extremely large amounts of computational time [13, 14]. Feulvarch et al. [15] and Dialami et al. [16] used the new moving mesh strategies to avoid remeshing. In the strategies, the mesh is partitioned into 3 parts: a first one which is fixed around the stirring zone, a second one which includes the base material in contact with the tool, and a third one (the tool). The coupling between each part can be performed using a node-to-node link approach, and only the connection between the moving and the fixed parts changes at each time step. Therefore, there are no mesh distortions and the formalism leads to satisfying computing time. The models adopting the Lagrangian methodology do not need the remeshing operations and demonstrate enormous advantages in computational costs and efficiency, especially for the cases in which only the thermal information is concerned [17, 18]. In all thermal models, one of the main tasks is to reveal the physical nature of FSW and give the appropriate analytical model for heat generation.

In the early stage, Chao and Qi [19] thought that the heat source generated by the friction at the shoulder/workpiece interface was the major one and assumed that the downward pressure from the tool distributed uniformly at the interface. The authors built the relationship between the surface heat flux and the pressure based on the classical Coulomb's friction law. Song and Kovacevic [20] assumed that the heat at the tool/workpiece interface was only caused by friction, and the friction coefficient was constant. The heat from the tool pin was taken into account and divided into three parts: (1) heat generated by shearing of the material; (2) heat generated by the friction on the threaded surface of the pin; and (3) heat generated by the friction on the vertical surface of the pin. Zhang et al. [17] proposed an analytical model for heat generation during the plunging stage, and the heat flux generated by the friction at the pin/workpiece interface is applied as volume heat. Khandkar et al. [21] assumed a uniform shear stress at the tool/workpiece interface and built a correlation between the moving heat flux and the actual machine power input. Schmidt et al. [22] established an analytical model for heat generation based on the modified Coulomb's friction law. Three contact conditions at the tool/workpiece interface including sliding, sticking, and partial sliding/sticking are defined to describe the respective mechanisms of heat generation. The experimental results demonstrated that the sticking or close to sticking condition was present at the tool/workpiece interface.

However, some common problems remain unsolved in the above-mentioned analytical model. First, the volumetric heat flux was considered to distribute uniformly in the pin volume, and it was discrepant with the real FSW process. Second, only a few authors revealed the temperature field in the plunge stage and always set the tilt angle of the FSW tool to be zero for simplicity, which brings about some simulating deviation. The analytical model, in which the volumetric heat flux distributes uniformly in the pin volume and the tilt angle is neglected, is called the conventional analytical model (CAM). A modified analytical model (MAM) in the current research was developed to consider the nonuniform volumetric heat flux and the tilt angle. Two analytical models are adopted in this paper to describe the specific heat generation, and the temperature fields including the temperature distribution and thermal cycle were compared to identify the simulating accuracy. This work can help the investigation on the physical nature of heat generation and can contribute to the numerical studies on FSW. In order to justify the analytical models, the AA6005A-T6 aluminum hollow extrusions were friction stir welded, and the comparisons between measured and numerical results in the CAM and MAM were analyzed in this work.

2. Experimental and Numerical Details

2.1. Experimental Details. The AA6005A-T6 aluminum hollow extrusions with a butting depth of 4 mm were friction stir welded. The tool was composed of a shoulder with the scrolled feature and a right-hand conical screwed pin, as shown in Figure 1. The tool shoulder radius R_0 was 10 mm, and an Archimedes scrolled groove was made on the flat shoulder. The root radius R_1 and length H of the pin are 4 mm and 3.8 mm, respectively, and the right-hand threads and three flutes were machined on the pin side to promote the material flow. The welding experiments were conducted on the ESAB SuperStir™ FSW machine, as shown in Figure 2. The process parameters in different stages were listed in Table 1. The transient temperatures at 5 locations were recorded using K-type thermocouples embedded into the predrilled holes, and the locations of thermocouples (or holes) were shown in Figure 3. The depth and diameter of each hole were 2.0 mm and 1.0 mm, respectively.

2.2. Numerical Details. It should be noted that the analytical model only expounds the mechanism of heat generation, and it must be implemented in numerical software in order to analyze the temperature field. In this paper, the commercial FEA software MSC. MARC, which is a Lagrangian implicit code, is used to model the FSW. Two hollow extrusions are meshed due to the structural asymmetry, and the detailed mesh generation is shown in Figure 4. In order to balance the computational accuracy

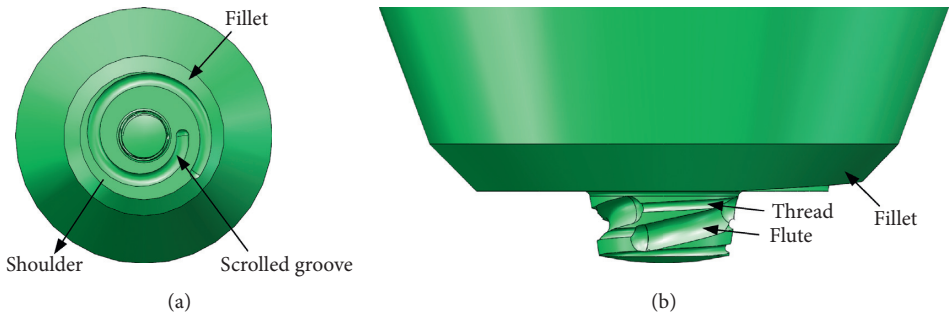

Figure 1: The tool used in welding experiments. (a) Vertical view; (b) front view.

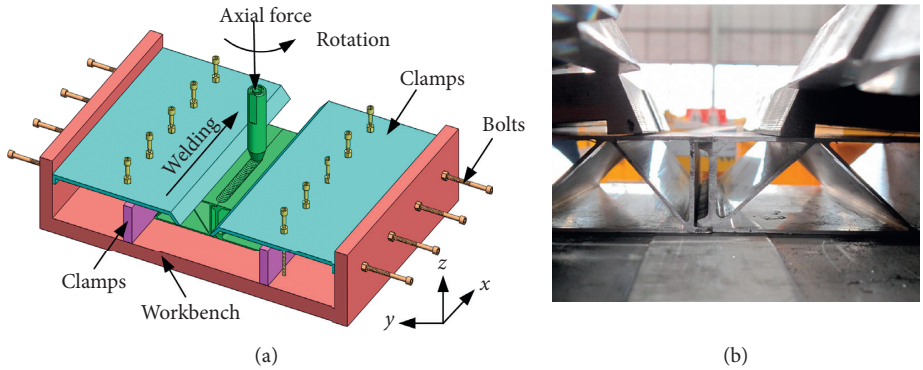

Figure 2: High-speed friction stir welding process. (a) Schematic view; (b) experimental setup.

Table 1: Welding parameters in different stages during the FSW process.

Stage	Rotation speed (rpm)	Plunge/traverse speed (mm/min)	Plunge depth (mm)	Tilt angle (°)
Plunge	600	24	0.4	1.5
Traverse	1000	1000		

and efficiency, the dimensions of meshes in A zone including the weld zone are 1 mm × 1 mm × 1 mm, and the meshes in B (B1 and B2) and C (C1 and C2) zones will gradually become coarser along the transverse direction (TD) and normal direction (ND) except the welding direction (WD). The finite thermal model consists of 212, 700 elements and 266, 686 nodes.

As a three-dimension quasisteady heat transfer process, the governing equation for thermal conduction in Cartesian coordinates in FSW can be written as follows:

$$\frac{\partial}{\partial x}\left(k(T)\frac{\partial T}{\partial x}\right)+\frac{\partial}{\partial y}\left(k(T)\frac{\partial T}{\partial y}\right)+\frac{\partial}{\partial z}\left(k(T)\frac{\partial T}{\partial z}\right)+q(x,y,z,t)=\rho(T)c(T)\frac{\partial T}{\partial t}, \quad (1)$$

where $k(T)$ is the thermal conductivity, $q(x,y,z,t)$ is the inner heat generation rate per unit volume, $\rho(T)$ is the mass density, and $c(T)$ is the specific heat.

The convection boundary condition for all the surfaces of the workpiece is as follows [23]:

$$k(T)\left.\frac{\partial T}{\partial n}\right|_{\Gamma}=h(T-T_0), \quad (2)$$

where n is the normal direction vector of the boundary Γ, h is the heat convection coefficient, and T_0 is the ambient temperature. The heat convection from the workpiece to the backing plate or clamps is complex and uncertain due to the contact gap conductance [21]. Therefore, the steel backing plate and clamps are removed in this model, and the corresponding contact surfaces are assumed to be cooled by convection from a cool fluid owning a heat convection coefficient of 500 $W{\cdot}m^{-2}{\cdot}^{\circ}C^{-1}$ [24, 25]. On the other surfaces, a heat convection coefficient of 30 $W{\cdot}m^{-2}{\cdot}^{\circ}C^{-1}$ is used to define the natural convection between the workpiece and air [26, 27]. The initial boundary condition describing the detailed value at a specific time can be expressed as follows:

$$T(x,y,z,t=0)=T_0. \quad (3)$$

The value of thermal-physical parameters at different temperatures are taken from [28, 29], and the relationship

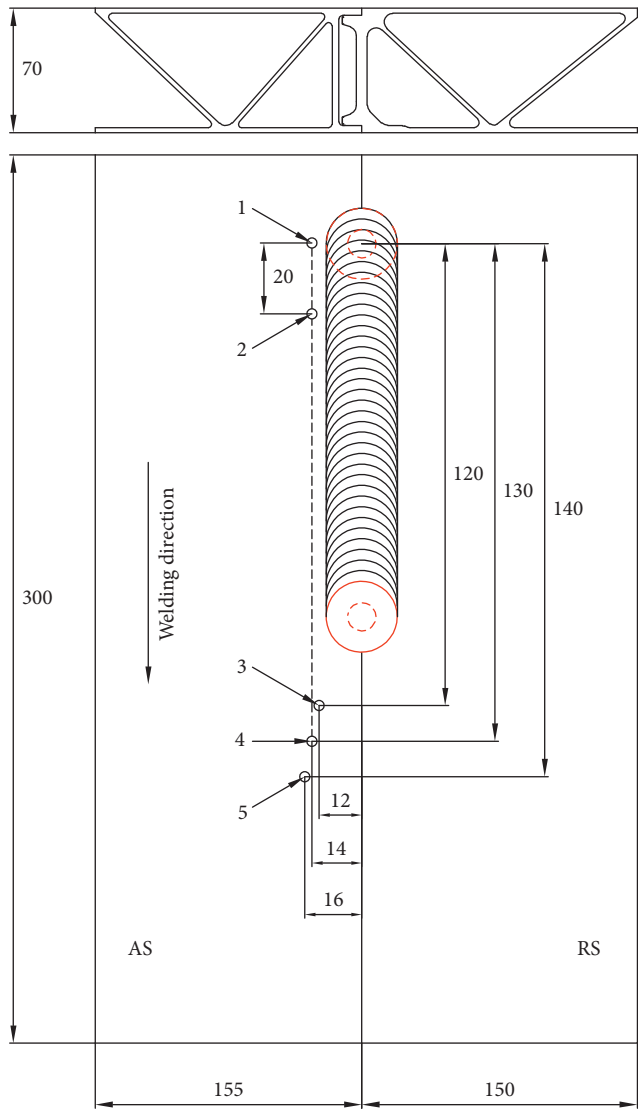

Figure 3: Dimensions of the workpiece and locations of the thermocouples. (Unit: mm).

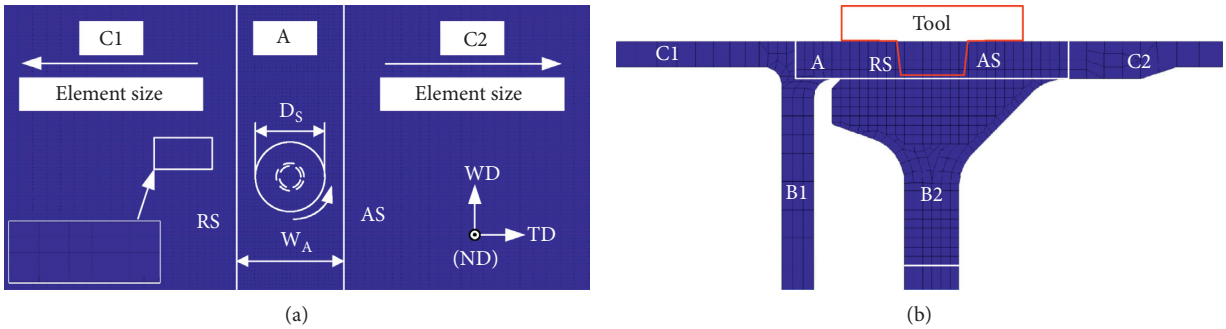

Figure 4: Grid mesh of the established thermal model in different views. (a) Top view; (b) front view.

between each parameter and temperature can be deduced as follows:

$$k(T) = 0.05121 \times T + 116.2 \left(W \cdot m^{-1} \cdot {}^{\circ}C^{-1}\right), \quad (4)$$

$$c(T) = 3176 \times e^{-(T-5015/4467)^2} \left(J \cdot kg^{-1} \cdot {}^{\circ}C^{-1}\right), \quad (5)$$

$$\sigma(T) = 159.2 \times e^{-(T-19.22/347.7)^2} (MPa), \quad (6)$$

$$\rho(T) = 3139 \times e^{-(T+3934/9993)^2} \left(kg \cdot m^{-3}\right), \quad (7)$$

where $\sigma(T)$ is the yield strength. Plots of the thermophysical parameters given by equations (4)~(7) are shown in Figure 5.

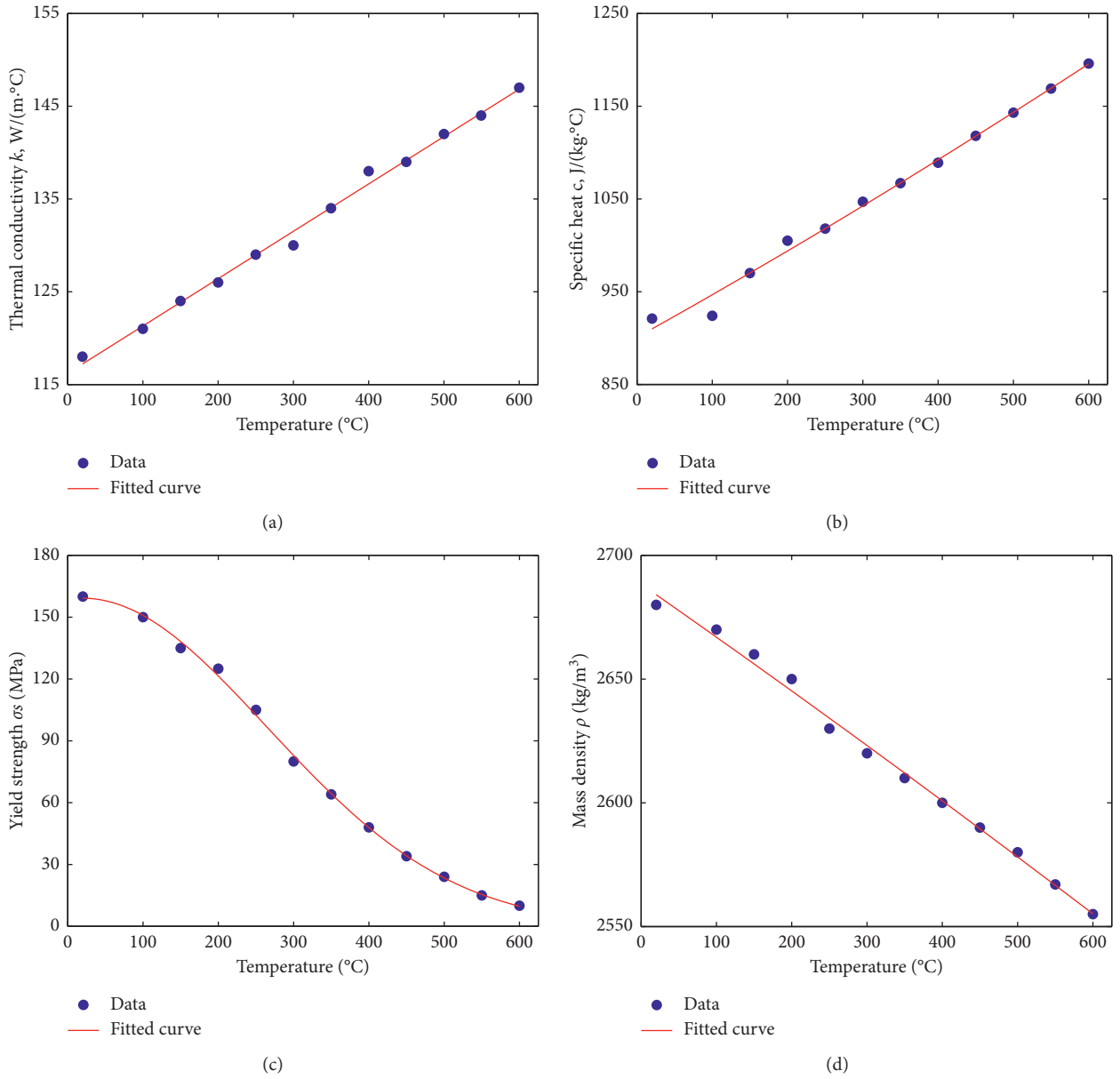

FIGURE 5: Thermophysical parameters used in the analytical model. (a) Thermal conductivity; (b) specific heat; (c) yield strength; (d) mass density.

3. Heat Generation

The heat generation from the friction and plastic deformation is governed by the contact condition between the tool and the workpiece, and a contact state variable δ is used to describe the different conditions:

$$\delta = \frac{\omega'}{\omega}, \tag{8}$$

where $\omega\prime$ and ω are the angular velocity of the matrix and the tool. $\delta = 0$ (full sliding) or $\delta = 1$ (full sticking) is not likely to occur at the tool/workpiece interface, and the actual value of δ is in the range of 0-1 (partial sliding/sticking) [30].

The analytical expression used for heat generation is established in the form of heat flux, and the total heat flux can be expressed as follows [31]:

$$q_{\text{total}} = q_{\text{friction}} + q_{\text{plastic}} = \omega r \tau_{\text{yield}}(T), \tag{9}$$

where r is the distance from the heat source center, and $\tau_{\text{yield}}(T)$ is the shear yield stress, which is equal to $\sigma(T)/\sqrt{3}$ according to the von Mises yield criterion.

3.1. Plunge Stage in the CAM. The plunge stage is subdivided into two stages: it is called the pin-plunging stage before the shoulder contacts with the workpiece, and the rest is called the shoulder-plunging stage. In the CAM, the volumetric heat flux (yellow zone) is assumed to distribute uniformly in the pin volume [32, 33], and the concrete distribution characteristics in the pin-plunging stage at different steps are illustrated in Figure 6. The maximum sectional radius r_s and the effective pin volume V_{ep} can be calculated as follows:

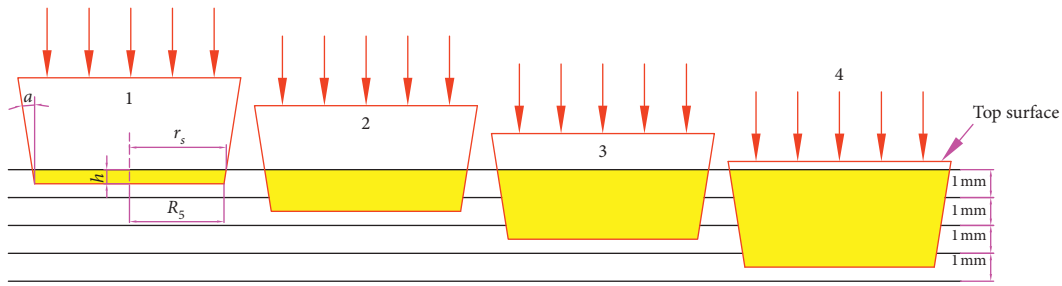

Figure 6: Distributions of the volumetric heat flux in the pin-plunging stage at different steps in the CAM.

$$r_s = R_5 + h \cdot \tan\alpha,$$
$$V_{ep} = \frac{1}{3}\pi h\left(r_s^2 + r_s R_5 + R_5^2\right), \tag{10}$$

where R_5 and α are the tip radius and semicone angle of the pin, respectively, and h is the transient plunge depth.

Figure 7 shows how to get an infinitesimal segment area on the pin surface, and the heat from the pin side Q_{ps} and pin tip Q_{pt} can be derived as follows:

$$Q_{ps} = \int_0^{2\pi}\int_{R_5}^{r_s} \omega r_1 \tau \cdot r_1 \mathrm{d}\theta_1 \frac{\mathrm{d}r_1}{\sin\alpha} = \frac{2\pi\omega\sigma}{3\sqrt{3}\sin\alpha}\left(r_s^3 - R_5^3\right),$$
$$Q_{pt} = \int_0^{2\pi}\int_{r_s}^{R_5} \omega r_5 \tau \cdot r_5 \mathrm{d}\theta_5 \mathrm{d}r_5 = \frac{2\pi\omega\sigma}{3\sqrt{3}} R_5^3, \tag{11}$$

where σ is the nodal yield strength. Then the volumetric heat flux q_p can be expressed as follows:

$$q_p = \frac{Q_{ps} + Q_{pt}}{V_{ep}} = \frac{2\omega\sigma}{\sqrt{3}\cos\alpha} + \frac{2\omega\sigma R_5^3}{\sqrt{3}h\left(r_s^2 + r_s R_5 + R_5^2\right)}. \tag{12}$$

It is well known that the heat generated from the shoulder plays a major role in the total heat generation, and the interaction between the shoulder and workpiece can significantly influence the temperature field in the plunge stage. In the CAM, the tilt angle is always considered to be zero for simplicity [34, 35], and the shoulder immediately contacts with the workpiece entirely once the pin reaches the target depth, which is inconsistent with the real FSW process. The contact conditions between the shoulder and workpiece in the shoulder-plunging stage at different steps are exhibited in Figure 8. The surface heat flux from the shoulder q_s can be described by equation (9)

$$q_s = \omega r \frac{\sigma_s}{\sqrt{3}}, \quad (R_1 \le r \le R_0), \tag{13}$$

where R_1 is the bottom radius of the pin, and R_0 is the radius of the shoulder. It should be noted that part of the heat at the shoulder/workpiece interface will "flow" into the tool, and the ratio of the heat "flow" into the workpiece can be calculated as follows [36]:

$$f = \frac{\sqrt{(k\rho c)_{\text{workpiece}}}}{\sqrt{(k\rho c)_{\text{tool}}}}. \tag{14}$$

In FSW of the 6XXX aluminum alloys, the temperature at the shoulder/workpiece interface is approximately in the range of 400-500°C [37, 38]. The thermal-physical parameters of the workpiece and the tool at 450°C are substituted to equation (14) and a value of 0.62 can be obtained. The surface heat flux from the shoulder can be expressed as follows:

$$q_s = f\omega r \frac{\sigma_s}{\sqrt{3}}, \quad (R_1 \le r \le R_0). \tag{15}$$

3.2. Traverse Stage in the CAM. As the tool moves forward, a micropore will occur and then is filled with the plasticized material in a short time, and the friction stir welding can be regarded as micropores generation and disappearing [39]. Therefore, only about half of the pin works to generate the heat [40], and the volumetric heat flux q_p can be given by equation (12):

$$q_p = \frac{\omega\sigma}{\sqrt{3}\cos\alpha} + \frac{\omega\sigma R_5^3}{\sqrt{3}H\left(R_1^2 + R_1 R_5 + R_5^2\right)}, \tag{16}$$

where H is the pin length.

The surface heat flux is calculated by using equation (15).

3.3. Plunge Stage in the MAM. It can be seen from equation (12) that the volumetric heat flux in the CAM depends on only the yield strength and transient plunge depth, and the values of all nodes are calculated using the same equation. However, the heat flux of each node varies with the distance from the heat source center (see equation (9)), and the hypothesis of uniform volumetric heat flux will bring an error about the prediction of the nodal temperature. So, a modified analytical model is developed in the current research to reduce the error. Specifically, the volumetric heat flux (color zone) is segmented into several parts in the pin-plunging stage at different steps ($i = 1 - 4$), as depicted in Figure 9. The bottom radius of the j layer r_j can be given as follows:

$$r_j = R_5 + (h - j + 1) \cdot \tan\alpha, \quad (j = 1 - 4). \tag{17}$$

Figure 10 illustrates how to get an infinitesimal segment area on the pin surface. The heat generation of the j layer

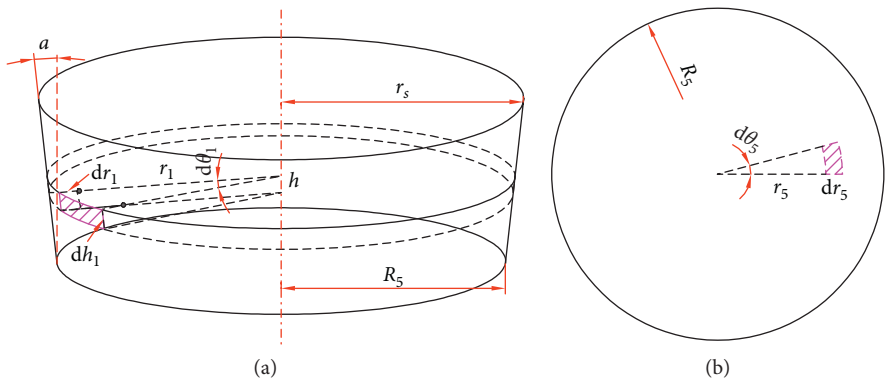

Figure 7: Infinitesimal segment areas from the pin surface in the CAM. (a) Pin side; (b) pin tip.

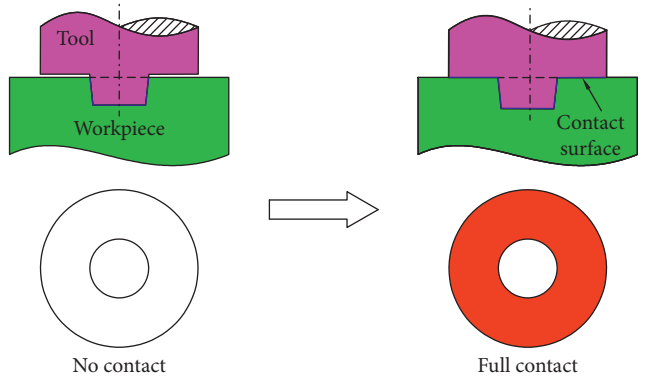

Figure 8: Contact conditions between the shoulder and workpiece in the shoulder-plunging stage at different steps in the CAM.

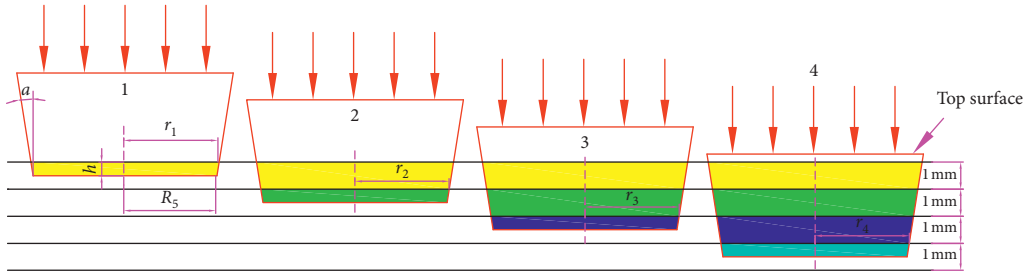

Figure 9: Distributions of the volumetric heat flux in the pin-plunging stage at different steps in the MAM.

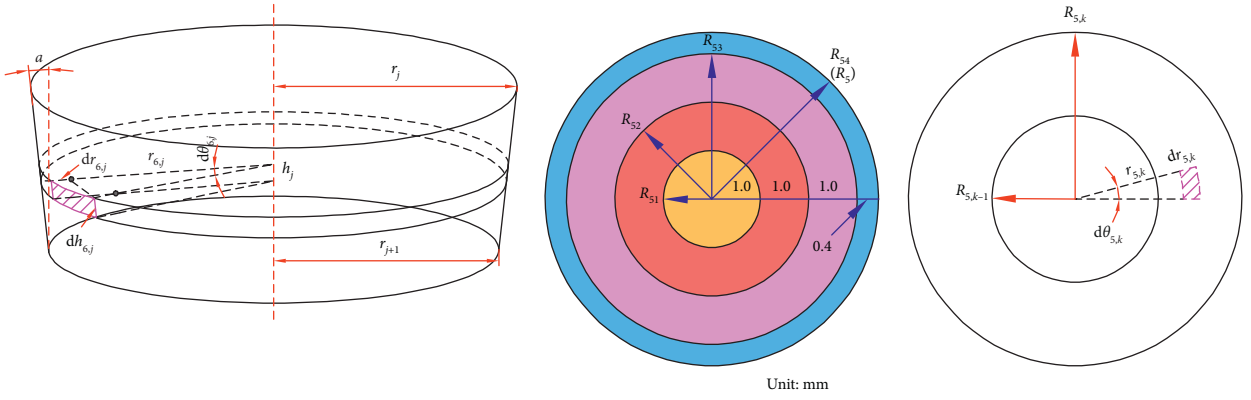

Figure 10: Infinitesimal segment areas from the pin surface in the MAM. (a) Pin side; (b) pin tip.

from the pin side at the i step Q_{psj} can be calculated via equation (9):

$$Q_{\mathrm{psj}} = \begin{cases} \int_0^{2\pi} \int_{r_{j+1}}^{r_j} \omega r_{6,j} \tau_{ij} \cdot r_{6,j} \mathrm{d}\theta_{6,j} \dfrac{\mathrm{d}r_{6,j}}{\sin\alpha} = \dfrac{2\pi\omega\sigma_{ij}}{3\sqrt{3}\,\sin\alpha}\left(r_j^3 - r_{j+1}^3\right), & (j < i), \\ \int_0^{2\pi} \int_{R_5}^{r_j} \omega r_{6,j} \tau_{ij} \cdot r_{6,j} \mathrm{d}\theta_{6,j} \dfrac{\mathrm{d}r_{6,j}}{\sin\alpha} = \dfrac{2\pi\omega\sigma_{ij}}{3\sqrt{3}\,\sin\alpha}\left(r_j^3 - R_5^3\right), & (j = i), \end{cases} \tag{18}$$

where σ_{ij} is the yield strength from the j layer at the i step. The tip radius of the pin is 3.4 mm, and it is unreasonable to assign a constant yield strength for the whole area. The pin tip is divided into one circle and three concentric rings, as shown in Figure 10(b). In each circle or ring, the heat flux is assumed to be uniform. The heat generation in the k circle or ring Q_{ptk} can be expressed as follows:

$$Q_{\mathrm{ptk}} \begin{cases} \int_0^{2\pi} \int_0^{R_{5,k}} \omega r_{5,k} \tau_{5,k} \cdot r_{5,k} \mathrm{d}\theta_{5,k} \mathrm{d}r_{5,k} = \dfrac{2\pi\omega\sigma_{5,k}}{3\sqrt{3}} R_{5,k}^3, & (k = 1), \\ \int_0^{2\pi} \int_0^{R_{5,k}} \omega r_{5,k} \tau_{5,k} \cdot r_{5,k} \mathrm{d}\theta_{5,k} \mathrm{d}r_{5,k} = \dfrac{2\pi\omega\sigma_{5,k}}{3\sqrt{3}}\left(R_{5,k}^3 - R_{5,k-1}^3\right), & (k = 2-4), \end{cases} \tag{19}$$

where $\sigma_{5,k}$ and $R_{5,k}$ are the yield strength and radius of the k circle or ring, respectively.

Meanwhile, the pin volume of the j layer at the i step V_{ij} is as follows:

$$V_{ij} = \begin{cases} \dfrac{1}{3}\pi h j \left(\left(r_j^2 + r_j r_{j+1} + r_{j+1}^2\right)\right), & (j < i), \\ \dfrac{1}{3}\pi h j \left(r_j^2 + r_j R_5 + R_5^2\right), & (j = i), \end{cases} \tag{20}$$

where h_j is the height of the j layer. So, the volumetric heat flux of the j layer at the i step q_{ij} can be written as follows:

$$q_{ij} = \frac{Q_{\mathrm{psj}} + Q_{\mathrm{ptk}}}{V_{ij}} \begin{cases} \dfrac{2\omega\sigma_{ij}}{\sqrt{3}\cos\alpha}, & (j < i), \\ \dfrac{2\omega\sigma_{ij}}{\sqrt{3}\cos\alpha} + \dfrac{2\omega R_{51}^3\left(\sigma_{51} + 7\sigma_{52} + 19\sigma_{53} + 12.304\sigma_{54}\right)}{\sqrt{3h_j}\left(r_j^2 + r_j R_5 + R_5^2\right)}, & (j = i). \end{cases} \tag{21}$$

In fact, the pin volume V_{ij} is occupied by the pin and not the base material during FSW, and it is theoretically more accurate to use a surface heat flux on the pin surface while it is unable to apply a surface heat flux on the specific elements in the pin volume, and the assumption that the heat distributes uniformly in each layer inhibits the heat flux from transferring through the pin/workpiece interface. In other words, the base material in pin volume does not have a significant impact on the temperature distribution, and adopting the volumetric heat flux does not reduce the

simulating accuracy obviously. It is observed from equation (21) that the volumetric heat flux of each node is directly affected by the yield strength, and how to calculate the value of different layers is a key point. This equation only gives the mathematical form of the volumetric heat flux, and how to calculate its value and apply the value to the specific elements in the MARC software will be elaborated in the following.

In view of computational cost and efficiency, the meshes cannot be refined infinitely. The butting depth is 4 mm, and the weld zone can be divided into 4 layers of elements combined with 5 layers of nodes, as shown in Figure 11(a). When calculating the q_{ij} $(j<i)$, the average temperature of 8 nodes in the m layer $(m=j)$ is selected to deduce the yield strength according to equation (6), as shown in Figure 11(b). As for calculating the q_{ij} $(j=i)$ of the last layer, the yield strength from the side and tip of the pin needs to be considered. The calculation of the yield strength from the pin side is the same as other layers. The yield strength in each circle or ring from the pin tip is calculated using the average temperature of 4 nodes in the m layer and 4 nodes in the $m+1$ layer, as shown in Figure 11(c). For the convenience of programming, a set of numbering rules is set up to describe the node number. L and k are the distance of any node from the heat source center around the pin side and pin tip, respectively. Four directions $(d=1-4)$ are assigned for telling the difference among the nodes with the same L. For example, n_{jdL} represents the node L mm away from the heat source center at the d direction in the j layer, and n_{mdk} represents the node k mm away from the heat source center at the d direction in the m layer. Then the average temperature of the j layer from the pin side at the i step T_{ij} can be given as follows:

$$T_{ij}=\frac{1}{8}\left(n_{j,1,4}+n_{j,2,4}+n_{j,3,4}+n_{j,4,4}+n_{j,1,5}+n_{j,2,5}+n_{j,3,5}+n_{j,4,5}\right). \tag{22}$$

The average temperature in the k circle (or ring) from the pin tip T_{jk} can be given as follows:

$$T_{jk}=\frac{1}{8}\left(n_{m,1,k}+n_{m,2,k}+n_{m,3,k}+n_{m,4,k}+n_{m+1,1,k}+n_{m+1,2,k}+n_{m+1,3,k}+n_{m+1,4,k}\right). \tag{23}$$

Figure 12 depicts the contact conditions between the shoulder and workpiece in the shoulder-plunging stage at different steps. When the trailing edge of the shoulder just contacts with the workpiece, the heat only originates from the pin/workpiece interface. Then the heat starts to generate at the shoulder/workpiece interface when they are in contact with each other, and the proportion becomes more and more as the contact area (blue thick line and red zone) increases gradually until the shoulder contacts fully with the workpiece. The specific surface heat flux generated at the shoulder/workpiece interface can be directly described by equation (15). The specific area for heat production S_s can be given as follows:

$$S_s=0,\quad \left(t\le=\frac{H-R_0\cdot\sin\alpha}{\mathrm{IW}}\right), \tag{24}$$

$$S_s=\begin{cases} R_1<r=\sqrt{x^2+y^2}\le R_0, \\ -R_1\le x\le -R_0+\dfrac{\mathrm{IW}}{\sin\alpha}\cdot\left(t-\dfrac{H-R_0\cdot\sin\alpha}{\mathrm{IW}}\right), \\ \left(\dfrac{H-R_0\cdot\sin\alpha}{\mathrm{IW}}<t<\dfrac{H+R_0\cdot\sin\alpha}{\mathrm{IW}}\right), \\ z=0, \end{cases} \tag{25}$$

$$S_s=\begin{cases} R_1\le r=\sqrt{x^2+y^2}\le R_0, \\ z=0, \end{cases} \quad \left(t\ge\frac{H+R_0\cdot\sin\alpha}{\mathrm{IW}}\right), \tag{26}$$

where (x, y, z) is the coordinate of the welding center, and IW is the plunging speed.

3.4. Traverse Stage in the MAM. In the traverse stage, the pin can be divided into 4 parts, as shown in Figure 13(a). The volumetric heat fluxes of 1–3 layers are calculated via dividing the heat from the pin side by the volume of each layer; the heats from the side and tip of the pin are used to calculate the volumetric heat flux of 4 layers. As only about half of the pin contacts with the workpiece, six nodes in three directions (1, 3, and 4) are selected to deduce the average temperature for calculating the volumetric heat flux from the pin side of each layer, as shown in Figure 13(b). The bottom radius of the j layer R_j is as follows:

$$R_j=R_5+(H-j+1)\cdot\tan\alpha,\quad (j=1-4). \tag{27}$$

The volumetric heat flux of the j layer q_j can be summarized as follows:

$$q_j=\begin{cases} \dfrac{\omega\sigma_j}{\sqrt{3}\cos\alpha}, & (j=1-3), \\ \dfrac{\omega\sigma_j}{\sqrt{3}\cos\alpha}+\dfrac{\omega R_{51}^3\left(\sigma_{51}+7\sigma_{52}+19\sigma_{53}+12.304\sigma_{54}\right)}{\sqrt{3}\,h_j\left(R_j^2+R_jR_5+R_5^2\right)}, & (j=4). \end{cases} \tag{28}$$

The average temperature on the side of the j layer T_j can be described as follows:

$$T_j=\frac{1}{6}\left(n_{j,1,4}+n_{j,3,4}+n_{j,4,4}+n_{j,1,5}+n_{j,3,5}+n_{j,4,5}\right). \tag{29}$$

The average temperature in the k circle (or ring) of 4 layer T_k is given as follows:

$$T_k=\frac{1}{6}\left(n_{4,1,k}+n_{4,3,k}+n_{4,4,k}+n_{5,1,k}+n_{5,3,k}+n_{5,4,k}\right). \tag{30}$$

The surface heat flux can be written as equation (15). The specific area for heat production S_s can be given by equation (26).

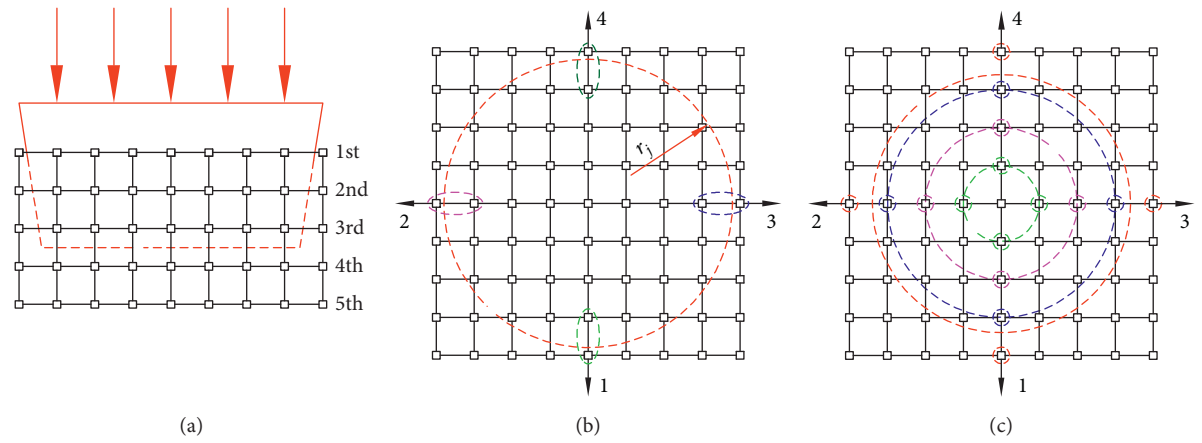

Figure 11: Grid mesh and node selection around the pin surface in the plunge stage in the MAM. (a) Division of elements and nodes; (b) node selection around the pin side; (c) node selection around the pin tip.

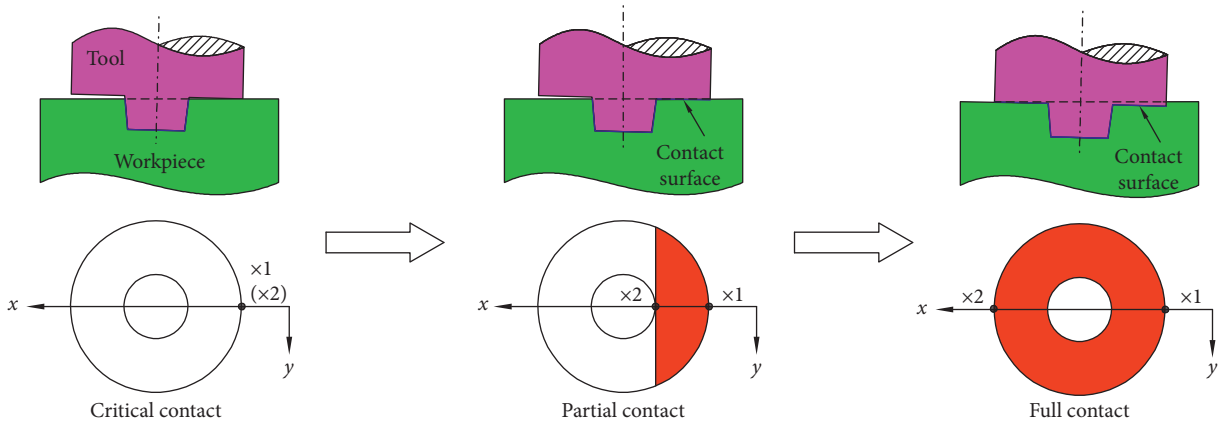

Figure 12: Contact conditions between the shoulder and workpiece in the shoulder-plunging stage at different steps in the MAM.

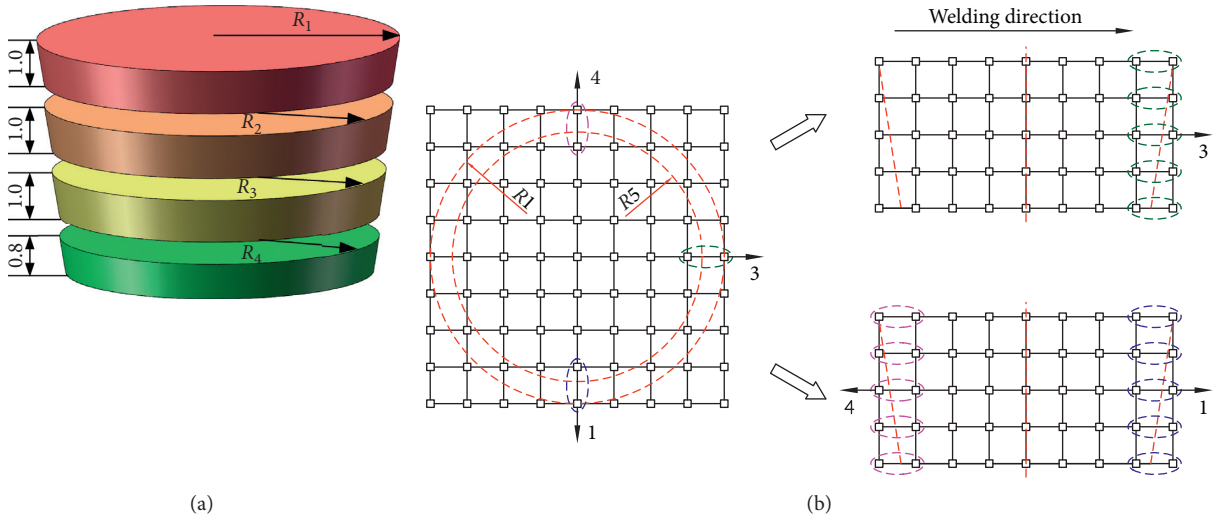

Figure 13: Pin division and node selection around the pin side in the traverse stage in the MAM. (a) Pin division; (b) node selection around the pin side.

4. Temperature Field

4.1. Model Verification. In order to verify the simulating precision of two thermal models, friction stir welding was carried out and the transient temperatures were recorded. Figure 14 shows the transient temperatures from the experimental measurement and numerical simulation in different stages. The numbers 1~5 in Figure 14 represent

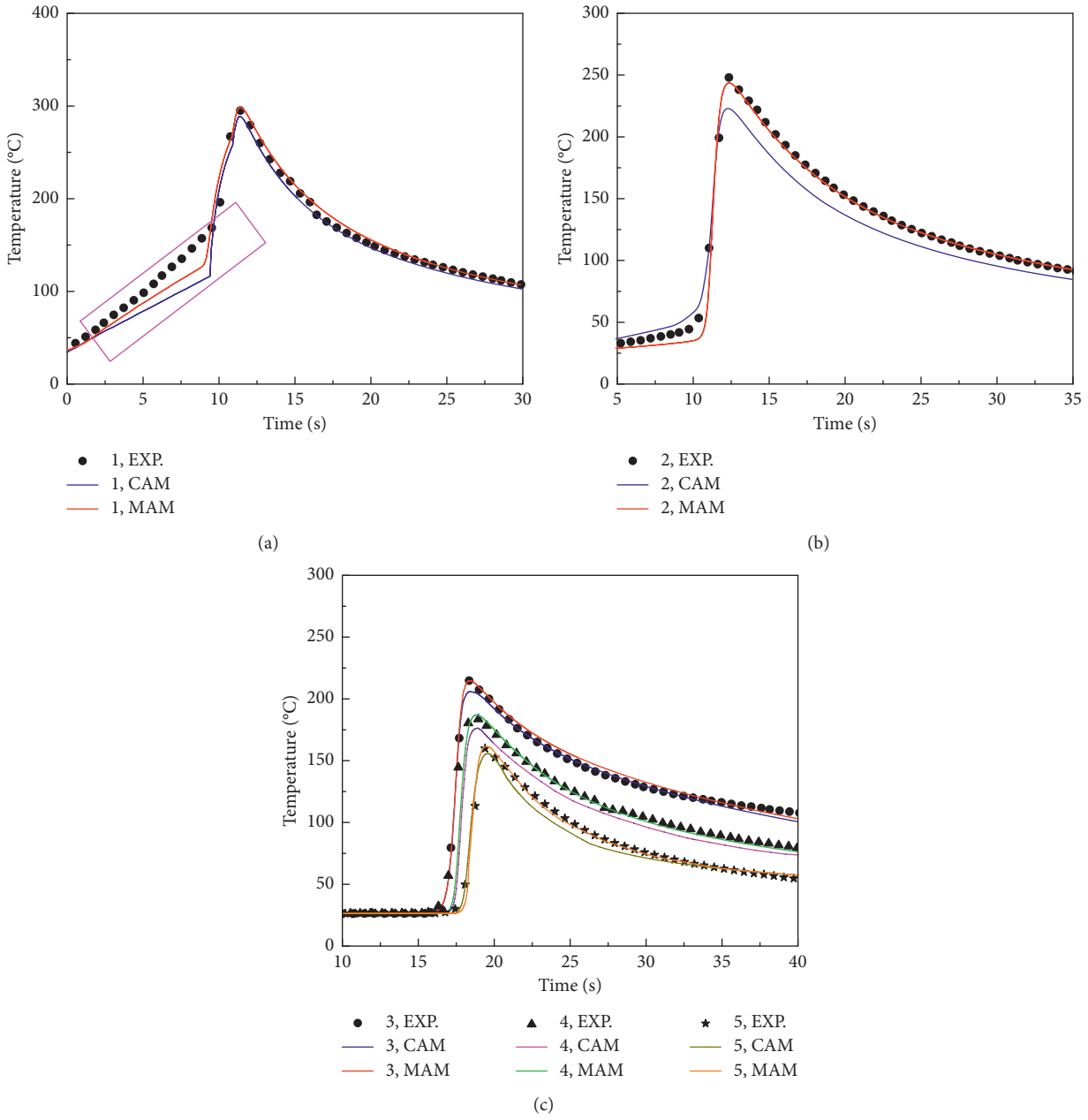

Figure 14: Comparison between the predicted and measured thermal cycles in different stages. (a) Plunge stage; (b) traverse stage (unsteady stage); (c) traverse stage (steady state).

the locations 1~5 in Figure 3, and the centers of location 1, location 2, and location 3~5 are located in the plunge stage, traverse stage (unsteady stage), and traverse stage (steady stage), respectively. Figure 14(a) shows that the heating rate in welding experiments is higher than that in the CAM and MAM during the plunge stage (0~11.55 s). This could be attributed to that the plunging pin gives rise to the "escaping" of the plasticized material from its original position in the actual welding process, and part of the material contacts with the shoulder to generate heat, which can increase the heating rate to some degree. Figure 14(b) shows the predicted and measured thermal cycles of location 2 in the traverse stage (unsteady stage). The maximum temperature in welding experiments is 248.1°C, and the maximum temperatures in the CAM and MAM are 230.0°C and 243.6°C, respectively. The predicted and measured thermal cycles of locations 3~5 in the traverse stage (steady stage) are shown in Figure 14(c). The simulated thermal cycles in the MAM show better agreement with the magnitude and shape of the experimental ones than that in the CAM.

The peak temperatures and the corresponding relative tolerances of locations 1~5 are revealed in Figure 15. The maximum temperature differences of the CAM and MAM are 25.2°C and 4.5°C, respectively. The relative tolerance between the predicted and measured value of the MAM are

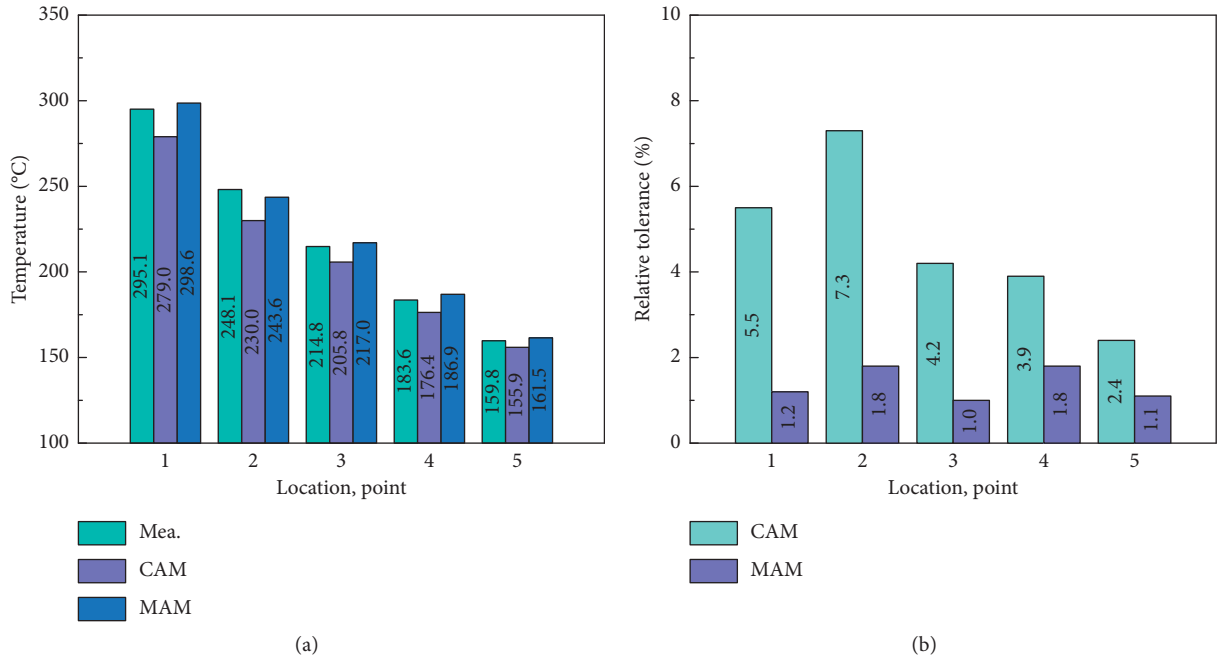

Figure 15: Comparison of the peak temperature and relative tolerance. (a) Peak temperature; (b) relative tolerance.

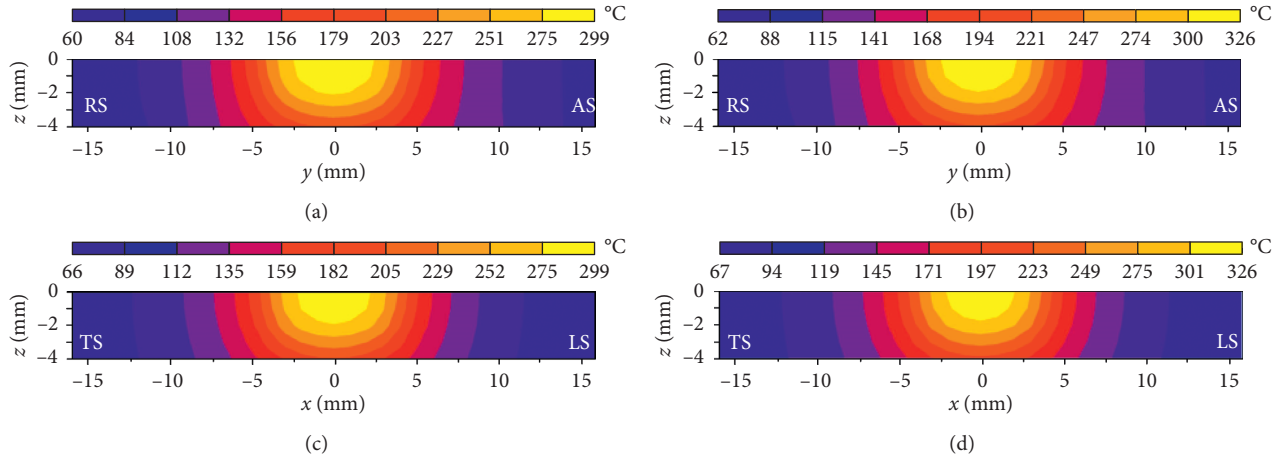

Figure 16: The predicted temperature distributions on different sections in the pin-plunging stage. (a) Transverse section in the CAM. (b) Transverse section in the MAM. (c) Longitudinal section in the CAM. (d) Longitudinal section in the MAM.

lower than that of the CAM, and the maximum value in the two models is 1.8% and 7.3%, respectively. These results demonstrate that the MAM owns a relatively higher simulating accuracy than that of the CAM.

4.2. Temperature Distribution. Figure 16 plots the calculated temperature distributions on the transverse sections (yoz, $x = 0$) and longitudinal sections (xoz, $y = 0$) in the pin-plunging stage. The temperature contour bands in the two models are different, and the maximum temperature in the MAM is 27.7°C higher than that in the CAM. The temperature difference between the CAM and MAM is mainly caused by the different calculating methods of the volumetric heat flux. During the pin-plunging stage, FSW results in intense plastic deformation around the rotating pin and friction between the pin and workpiece. That is to say, the heat is generated by plastic deformation and friction occurred in the region around the pin/workpiece interface. The region belongs to the low-temperature region in the stirred zone, and the corresponding yield strength is higher than in other regions. While in the CAM, the volumetric heat flux of each node which is mainly located in the high-temperature region is calculated using its own yield strength (temperature), and thus leads to the decrease of the volumetric heat flux. In the MAM, the average temperature at the pin/workpiece interface is used to calculate the volumetric heat flux of each node via equations (21)–(23), which can reflect a more accurate temperature distribution. Additionally,

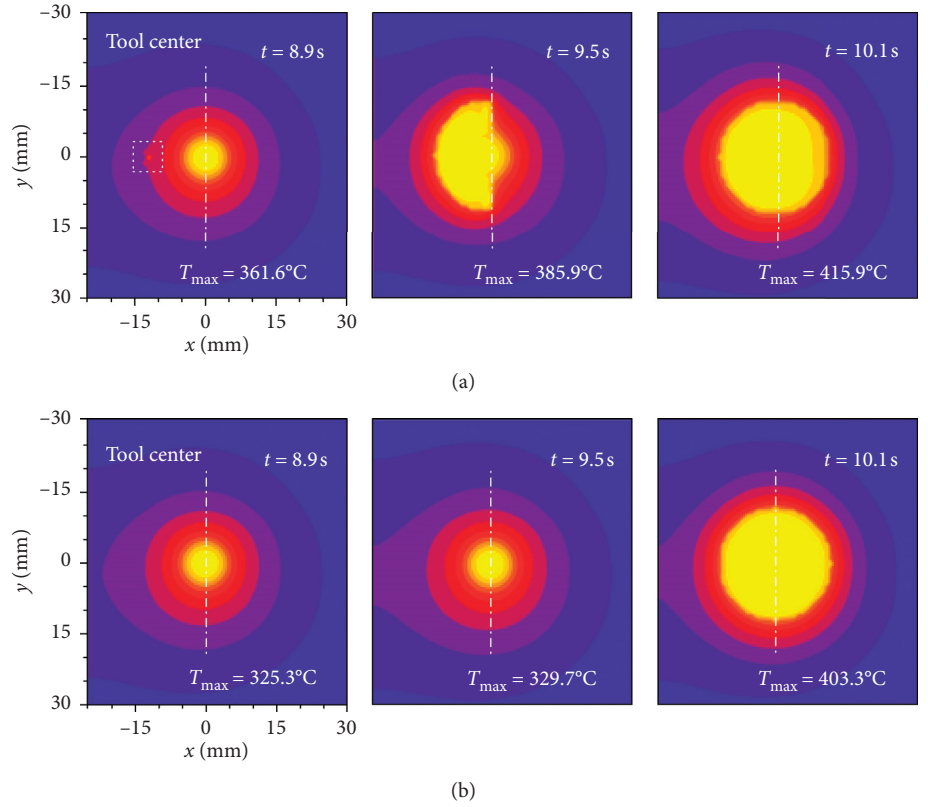

Figure 17: The predicted temperature distributions on the top surfaces in the shoulder-plunging stage in two models. (a) MAM; (b) CAM.

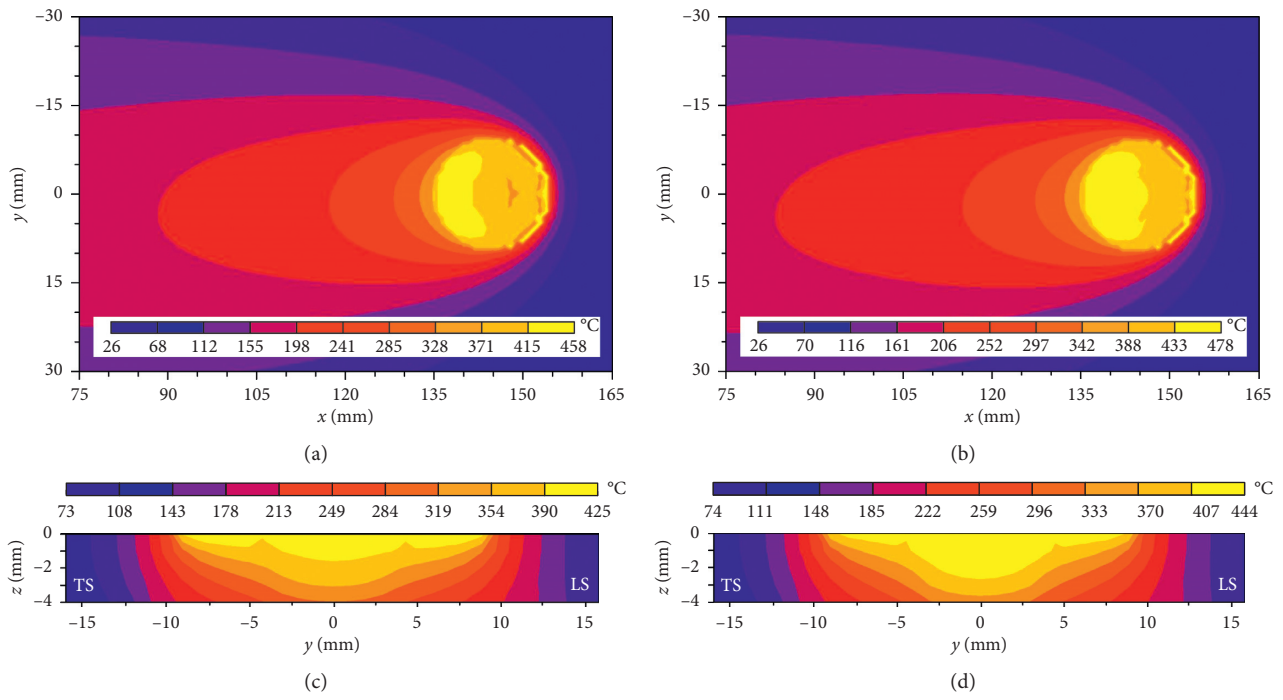

Figure 18: The predicted temperature distributions on different sections in the traverse stage. (a) Top surface in the CAM. (b) Top surface in the MAM. (c) Transverse section in the CAM. (d) Transverse section in the MAM.

some thermal characteristics in the two models are similar. The temperature distributions on the retreating side (RS) and advancing side (AS) are asymmetric about the weld center, and the temperature on the RS is relatively low and exhibits a high gradient, due to higher heat dissipation arising from the auxiliary rib. The opposite

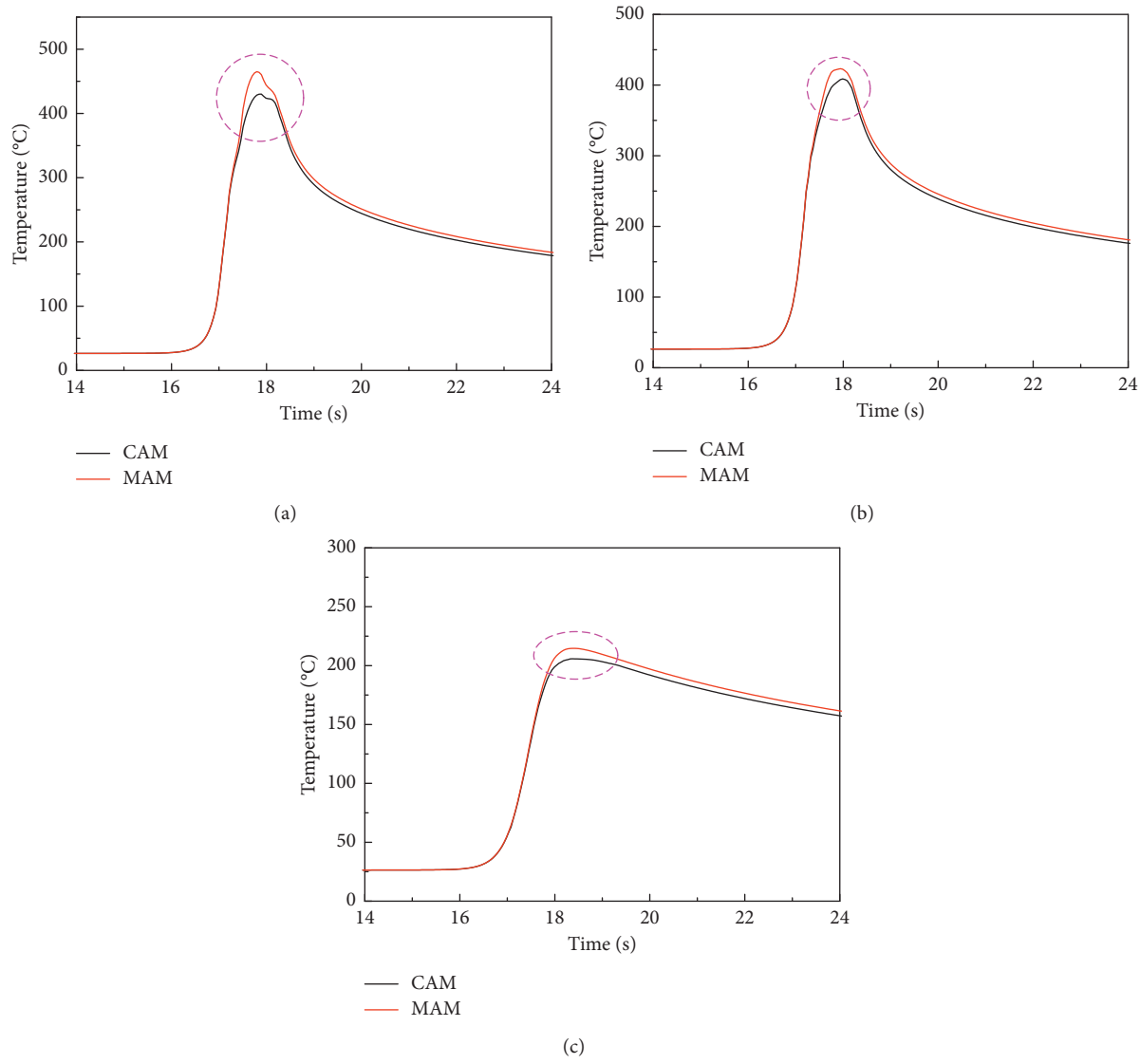

Figure 19: The predicted thermal cycles of different zones in the traverse stage. (a) NZ; (b) TMAZ; (c) HAZ.

thermal characteristics can be found on the trailing side (TS) and the leading side (LS) because of the gradual heat accumulation behind the tool.

Figure 17 depicts the temperature distributions on the tip surfaces in the shoulder-plunging stage at different times. When the pin plunges into the workpiece for 8.9 s in the MAM, the trailing edge of the shoulder contacts with the workpiece (white box in Figure 17(a)), and the maximum temperature is 361.6°C. At the 9.5 s, half of the shoulder contacts with the workpiece, and the maximum temperature increases to 385.9°C. When the time is 10.1 s, the shoulder contacts fully with the workpiece, and the resulting maximum temperature is 415.9°C. In contrast, the maximum temperature and heating rate in the CAM is significantly lower than that in the MAM before the shoulder contacts with the workpiece (10.1 s). In addition, the temperature distributions in the CAM and MAM are asymmetric with respect to the tool center, and the high-temperature zone (yellow zone) in the MAM is less uniform than that in the CAM. The phenomena result from two reasons. First, the *yoz* plane ($x = -25$) is the end surface exposed to air whose thermal conductivity is extremely low compared with the aluminum alloys, and the different cooling conditions on the two sides of the tool center cause the nonuniform temperature distribution in the two models. Second, the gradually plunging shoulder in the MAM leads to the nonuniform heat input on the two sides, which promotes the occurrence of the nonuniform temperature field, especially the high-temperature zone.

Figure 18 displays the temperature distributions on the tip surfaces and transverse sections across the tool center in the traverse stage. The temperature gradients in the front of the tool are much larger than that behind the tool, and the preheating width (WP) is only about 5 mm. The high-temperature zone is mainly located at the back of the tool due to the gradual accumulation of heat input. The maximum temperatures in the CAM and MAM are 457.8°C and 478.1°C, respectively. The peak temperatures on the transverse sections

in the two models are lower than the maximum temperature, and the values are 424.3°C and 444.1°C, respectively.

4.3. Thermal Cycle. Figure 19 shows the thermal cycles of different zones in the traverse stage, including nugget zone (NZ), thermomechanically affected zone (TMAZ), and heat affected zone (HAZ). It can be seen that the heating and cooling rates in the CAM and MAM are very similar, except the high-temperature regions that are marked by the purple ellipses. The heating rate is rather large, and the transient temperatures of different zones reach the peak value in 3 seconds; the cooling rate is much lower than the heating one, and the transient temperatures show a slowly decreasing trend. Additionally, the peak temperatures of three zones in the CAM are all lower than that in the MAM, especially that of NZ.

5. Conclusions

Two analytical models, including the conventional and modified models, are compared to describe the heat generation and predict the temperature field. The main conclusions are drawn as follows.

(1) In the modified analytical model, the nonuniform volumetric heat flux and the tilt angle of the tool are considered. The side and tip of the pin are divided into several parts, and the volumetric heat flux of each part is calculated separately, which can reflect a more accurate heat generation than that of the conventional one.

(2) Comparison of the predicted and measured thermal cycles and peak temperatures in two models demonstrates that the MAM owns a higher simulating accuracy than the CAM.

(3) In the pin-plunging stage, the temperature distributions in the two models are different, and the maximum temperature in the CAM is 27.7°C lower than that in the MAM. Meanwhile, some thermal characteristics are similar: the temperature distributions are asymmetric with respect to the weld center, and the temperatures on the RS and LS are lower than that on the AS and TS.

(4) In the shoulder-plunging stage, the maximum temperature and heating rate in the MAM are much higher than that in the CAM, but the distribution of the high-temperature region is less uniform.

(5) In the traverse stage, the high-temperature zone is mainly located at the back of the tool, and the peak temperature does not appear in the transverse section. The thermal cycles show that the peak temperature of different zones in the MAM are all higher than that in the CAM.

Data Availability

The data used to support the findings of this study are available from the corresponding author upon request.

Conflicts of Interest

The authors declare that there are no conflicts of interest regarding the publication of this paper.

Acknowledgments

The authors gratefully acknowledge the funding support received from the National Natural Science Foundation of China (Grant number: 51175117, U1404502) and the National Science and Technology Major Project of China (Grant number: 2010ZX04007-011).

References

[1] Z. H. Zhang, W. Y. Li, J. L. Li, and Y. J. Chao, "Effective predictions of ultimate tensile strength, peak temperature and grain size of friction stir welded AA2024 alloy joints," *The International Journal of Advanced Manufacturing Technology*, vol. 73, no. 9–12, pp. 1213–1218, 2014.

[2] V. Dixit, R. S. Mishra, R. J. Lederich, and R. Talwar, "Influence of process parameters on microstructural evolution and mechanical properties in friction stirred Al–2024 (T3) alloy," *Science and Technology of Welding and Joining*, vol. 14, no. 4, pp. 346–355, 2009.

[3] B. Abnar, M. Kazeminezhad, and A. H. Kokabi, "Effects of heat input in friction stir welding on microstructure and mechanical properties of AA3003–H18 plates," *Transactions of Nonferrous Metals Society of China*, vol. 25, no. 7, pp. 2147–2155, 2015.

[4] P. F. Mendez, K. E. Tello, and T. J. Lienert, "Scaling of coupled heat transfer and plastic deformation around the pin in friction stir welding," *Acta Materialia*, vol. 58, no. 18, pp. 6012–6026, 2010.

[5] C. Gao, Z. Zhu, J. Han, and H. Li, "Correlation of microstructure and mechanical properties in friction stir welded 2198–T8 Al–Li alloy," *Materials Science and Engineering: A*, vol. 639, pp. 489–499, 2015.

[6] P. Prasanna, B. S. Rao, and G. K. M. Rao, "Finite element modeling for maximum temperature in friction stir welding and its validation," *The International Journal of Advanced Manufacturing Technology*, vol. 51, no. 9–12, pp. 925–933, 2010.

[7] Z. Zhang and J. T Chen, "Computational investigations on reliable finite element–based thermomechanical– coupled simulations of friction stir welding," *The International Journal of Advanced Manufacturing Technology*, vol. 60, no. 12, pp. 959–975, 2012.

[8] P. A. Colegrove and H. R. Shercliff, "CFD modelling of friction stir welding of thick plate 7449 aluminum alloy," *Science and Technology of Welding and Joining*, vol. 11, no. 4, pp. 429–441, 2006.

[9] F. Al-Badour, N. Merah, A. Shuaib, and A. Bazoune, "Coupled Eulerian Lagrangian finite element modeling of friction stir welding processes," *Journal of Materials Processing Technology*, vol. 213, no. 8, pp. 1433–1439, 2013.

[10] Z. Yu, W. Zhang, H. Choo, and Z. Feng, "Transient heat and material flow modeling of friction stir processing of magnesium alloy using threaded tool," *Metallurgical and Materials Transactions A*, vol. 43, no. 2, pp. 724–737, 2012.

[11] H. Atharifar, D. Lin, and R. Kovacevic, "Numerical and experimental investigations on the loads carried by the tool

during friction stir welding," *Journal of Materials Engineering and Performance*, vol. 18, no. 4, pp. 339–350, 2009.

[12] G. Chen, Z. Feng, Y. Zhu, and Q. Shi, "An alternative frictional boundary condition for computational fluid dynamics simulation of friction stir welding," *Journal of Materials Engineering and Performance*, vol. 25, no. 9, pp. 4016–4023, 2016.

[13] G. Buffa, J. Hua, R. Shivpuri, and L. Fratini, "A continuum based fem model for friction stir welding–model development," *Materials Science and Engineering: A*, vol. 419, no. 1-2, pp. 389–396, 2006.

[14] H. Schmidt and J. Hattel, "A local model for the thermomechanical conditions in friction stir welding," *Modelling and Simulation in Materials Science and Engineering*, vol. 13, no. 1, pp. 77–93, 2005.

[15] E. Feulvarch, J.-C. Roux, and J.-M. Bergheau, "A simple and robust moving mesh technique for the finite element simulation of friction stir welding," *Journal of Computational and Applied Mathematics*, vol. 246, pp. 269–277, 2013.

[16] N. Dialami, M. Chiumenti, M. Cervera, and C. Agelet de Saracibar, "An apropos kinematic framework for the numerical modeling of friction stir welding," *Computers & Structures*, vol. 117, pp. 48–57, 2013.

[17] H. Zhang, J. H. Huang, S. B. Lin, L. Wu, and J. G. Zhang, "Temperature simulation of the preheating period in friction stir welding based on the finite element method," *Proceedings of the Institution of Mechanical Engineers Part B: Journal of Engineering Manufacture*, vol. 220, no. 7, pp. 1097–1106, 2006.

[18] X. K. Zhu and Y. J. Chao, "Numerical simulation of transient temperature and residual stresses in friction stir welding of 304L stainless steel," *Journal of Materials Processing Technology*, vol. 146, no. 2, pp. 263–272, 2004.

[19] Y. J. Chao and X. Qi, "Heat transfer and thermo–mechanical analysis of friction stir joining of AA6061–T6 plates," in *Proceedings of the 1st International Symposium on Friction Stir Welding*, Thousand Oaks, CA, USA, June 1999.

[20] M. Song and R. Kovacevic, "Thermal modeling of friction stir welding in a moving coordinate system and its validation," *International Journal of Machine Tools and Manufacture*, vol. 43, no. 6, pp. 605–615, 2003.

[21] M. Z. H. Khandkar, J. A. Khan, and A. P. Reynolds, "Prediction of temperature distribution and thermal history during friction stir welding: input torque based model," *Science and Technology of Welding and Joining*, vol. 8, no. 3, pp. 165–174, 2003.

[22] H. Schmidt, J. Hattel, and J. Wert, "An analytical model for the heat generation in friction stir welding," *Modelling and Simulation in Materials Science and Engineering*, vol. 12, no. 1, pp. 143–157, 2004.

[23] V. Soundararajan, S. Zekovic, and R. Kovacevic, "Thermomechanical model with adaptive boundary conditions for friction stir welding of Al 6061," *International Journal of Machine Tools and Manufacture*, vol. 45, no. 14, pp. 1577–1587, 2005.

[24] A. Aziz, "A similarity solution for laminar thermal boundary layer over a flat plate with a convective surface boundary condition," *Communications in Nonlinear Science and Numerical Simulation*, vol. 14, no. 4, pp. 1064–1068, 2009.

[25] Y. J. Chao and X. Qi, "Thermal and thermo–mechanical modeling of friction stir welding of aluminum alloy 6061–T6," *Journal of Materials Processing & Manufacturing Science*, vol. 7, no. 2, pp. 215–233, 1998.

[26] A. Bastier, M. H. Maitournam, K. Dang Van, and F. Roger, "Steady state thermomechanical modelling of friction stir welding," *Science and Technology of Welding and Joining*, vol. 11, no. 3, pp. 278–288, 2006.

[27] D. Jacquin, B. de Meester, A. Simar, D. Deloison, F. Montheillet, and C. Desrayaud, "A simple Eulerian thermomechanical modeling of friction stir welding," *Journal of Materials Processing Technology*, vol. 211, no. 1, pp. 57–65, 2011.

[28] T. Y. Zhang and H. Chen, "Numerical simulation of laser welding for different thickness aluminum alloy plate," *Advanced Materials Research*, vol. 391-392, pp. 642–647, 2011.

[29] A. Simar, J. Lecomte-Beckers, T. Pardoen, and B. de Meester, "Effect of boundary conditions and heat source distribution on temperature distribution in friction stir welding," *Science and Technology of Welding and Joining*, vol. 11, no. 2, pp. 170–177, 2006.

[30] H. N. B. Schmidt, T. L. Dickerson, and J. H. Hattel, "Material flow in butt friction stir welds in AA2024–T3," *Acta Materialia*, vol. 54, no. 4, pp. 1199–1209, 2006.

[31] J. Hilgert, H. N. B. Schmidt, J. F. dos Santos, and N. Huber, "Thermal models for bobbin tool friction stir welding," *Journal of Materials Processing Technology*, vol. 211, no. 2, pp. 197–204, 2011.

[32] Y. H. Yau, A. Hussain, R. K. Lalwani, H. K. Chan, and N. Hakimi, "Temperature distribution study during the friction stir welding process of Al2024-T3 aluminum alloy," *International Journal of Minerals, Metallurgy, and Materials*, vol. 20, no. 8, pp. 779–787, 2013.

[33] V. S. Gadakh and K. Adepu, "Heat generation model for taper cylindrical pin profile in FSW," *Journal of Materials Research and Technology*, vol. 2, no. 4, pp. 370–375, 2013.

[34] D. Veljic, M. Rakin, M. Perovic et al., "Heat generation during plunge stage in friction stir welding," *Thermal Science*, vol. 17, no. 2, pp. 489–496, 2013.

[35] H. Bisadi, S. Rasaee, and M. Farahmand, "Thermal analysis of plunge stage in friction stir welding: simulation and experiment," *International Journal of Basic Sciences and Applied Research*, vol. 2, no. 11, pp. 968–975, 2013.

[36] R. Nandan, G. G. Roy, T. J. Lienert, and T. Debroy, ""Three–dimensional heat and material flow during friction stir welding of mild steel," *Acta Materialia*, vol. 55, no. 3, pp. 883–895, 2007.

[37] Z. Zhang and Q. Wu, "Analytical and numerical studies of fatigue stresses in friction stir welding," *The International Journal of Advanced Manufacturing Technology*, vol. 78, no. 9–12, pp. 1371–1380, 2015.

[38] M. Riahi and H. Nazari, "Analysis of transient temperature and residual thermal stresses in friction stir welding of aluminum alloy 6061–T6 via numerical simulation," *The International Journal of Advanced Manufacturing Technology*, vol. 55, no. 1–4, pp. 143–152, 2011.

[39] H. Zhang, S. B. Lin, L. Wu, J. C. Feng, and S. L. Ma, "Defects formation procedure and mathematic model for defect free friction stir welding of magnesium alloy," *Materials & Design*, vol. 27, no. 9, pp. 805–809, 2006.

[40] H.-J. Zhang, H.-J. Liu, and L. Yu, "Thermal modeling of underwater friction stir welding of high strength aluminum alloy," *Transactions of Nonferrous Metals Society of China*, vol. 23, no. 4, pp. 1114–1122, 2013.